university of groningen / faculty of science and engineering

Heterogeneity of VELO's pixels response to a monochromatic Fe55 radioactive source

Abstract

With the purpose of computing the impact parameters and primary and secondary vertices of proton-proton collisions, the Vertex Locator (VELO) at the Large Hadron Collider beauty experiment has been recently replaced by a new silicon pixel version, set to measure the passage of charged particles. Currently, the pixels in the VELO need to be calibrated. In this study, the heterogeneity of the VELO's pixels, the nature of their discrepancy and the next steps for a proper calibration are investigated. By studying the charged particle flux spectra on each pixel, resultant from a monochromatic Fe55 radiation source, it is found that the individual spectra of the pixels significantly differ from that of the average spectrum. This is presumably due to the small resolution of the pixels, which is increased by six orders of magnitude when examining the average spectrum. Moreover, on account of the fact that no more than 15% of the pixels could be mathematically described, much longer exposure times to a radioactive source are justified to obtain more data and properly calibrate the pixels individually.

Author
Lucas van der Horst

Supervisor and first examiner
Dr. K.A.M. De Bruyn

Second examiner
Prof. Dr. S. Hoekstra

The Netherlands
July 7, 2023

Contents

1 Introduction

The earliest trace of wonder about the functioning and fundamental structure of nature and the universe dates from six centuries BC [1, p. 6], considered the birth of Western philosophy. Over two millennia of thinking and experimenting later, J.J. Thomson made the first discovery of an elementary particle in 1897: the electron [2]. The field of particle physics further matured in the succeeding years, discovering new particles and developing quantum theories. Finally, the term Standard Model (SM) emerged in 1975 to encompass the field, coined by S. Treiman and A. Pais [3], giving birth to modern particle physics. Almost five decades later, the SM is the best theory explaining how the Universe operates, describing seventeen elementary particles and three fundamental forces. At present day, particle physics has a cardinal impact on society and its functioning, finding its applications in big industries like medicine and healthcare, through technological developments such as positron emission tomography, proton and carbon-ion therapy, and radioisotopes production; materials science and nanotechnology, by enabling the development of novel materials, like superconductors, and high precision nanoengineering; and the energy sector, by way of advancing nuclear energy production and energy storage technologies.

Multiple open questions remain in particle physics that the SM cannot answer, notwithstanding its vast success. Some of its main limitations include its inability to be unified with General Relativity; to explain dark matter and dark energy; to account for the asymmetry between matter and antimatter, also known as the baryon asymmetry problem; to justify the evidence for massive neutrinos [4, 5], despite its contrary prediction; and to describe the mechanism that allows for the incredible lightness of the Higgs boson, the large discrepancy between the masses of the charged leptons and between the strength of gravity and the other fundamental forces, known as the hierarchy problem. Precision measurements of particle's properties and SM parameters, theoretical modeling and development of new frameworks, and studying the aforementioned phenomena is critical to obtain hints of physics beyond the SM.

The scientific community is devoting promising efforts into different studies with that purpose. Notable examples are the precision measurement of the muon's anomalous magnetic dipole moment measurement at Fermilab (see [6]) and of other fundamental constants; neutrino experiments, such as the Super-Kamiokande and the IceCube experiments; and the experiments done with particle accelerators, such as at the European Organization for Nuclear Research (CERN).

Among the nine experiments employing the largest and most powerful particle accelerator, the Large Hadron Collider (LHC) at CERN, is the LHC beauty (LHCb) experiment. Approved in 1998 and built in 2008, it is set to investigate the matter-antimatter asymmetry. Before reaching the rest of the LHCb detector, particles produced by the colliding protons (pp) travel first through the Vertex Locator (VELO), shown schematically in Fig. 1. For further details on the history, technical aspects and achievements of the LHCb see [7].

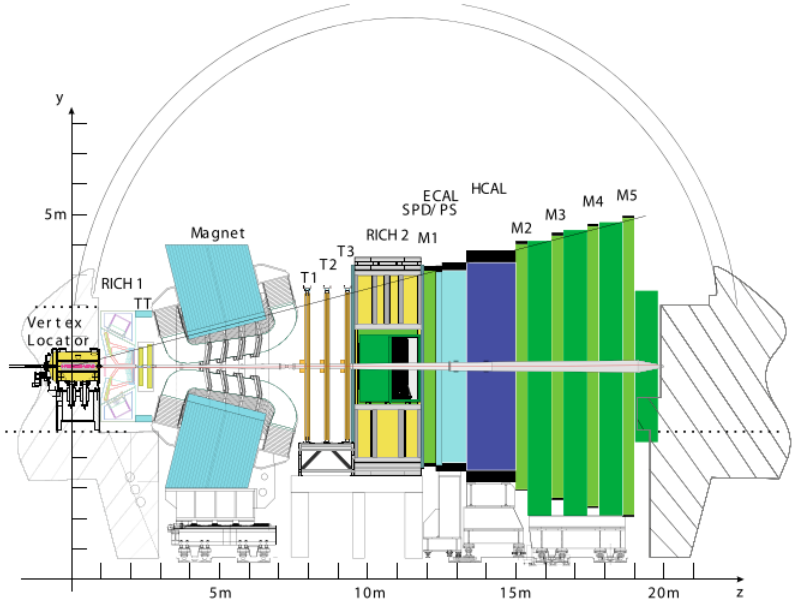

Figure 1: Schematic of the LHCb detector viewed sideways [8]. The VELO is located on the left.

1.1 The Vertex Locator

Replaced by a silicon pixel version during the Long Shutdown 2 (2018-2022) of the LHC, the VELO's purpose is to measure the passage of charged particles. Using this information, the impact parameter and location of the primary and secondary vertices of the pp interaction are calculated by means of a track reconstruction algorithm, which are figures needed by the LHCb for their investigations. To measure the passing of the charged particles, the VELO comprises 52 modules carrying 12 VeloPix application-specific integrated circuits (ASIC) consisting of a 256x256 grid of 55x55 μm^2 silicon-based pixels. See [9] for more technical information on the VeloPix ASIC and [8] for more details on the VELO upgrade. Fig. 2 depicts a schematic of the VELO. Charged particles traveling through a silicon pixel will ionize the material, generating a measurable current. The pixel is responsible for measuring a hit if a set threshold, to filter out the noise, is crossed. The crux lies in the fact that the pixels are not identical, owing to slight differences in sizes, electronics or material impurities, and, thereupon, have different sensitivities, potentially presenting obstacles in the calibration process.

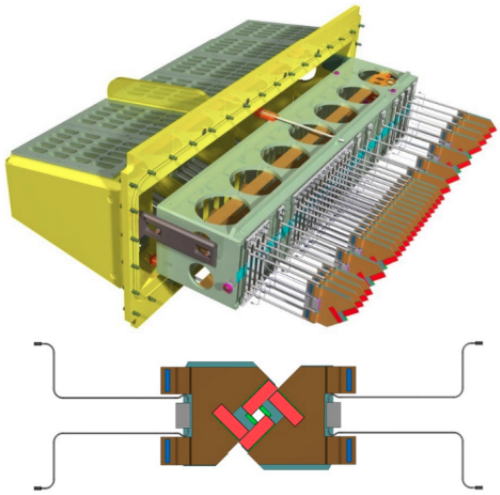

Figure 2: (Top) One half of the upgraded VELO detector. (Bottom) Two closed modules [8].

To properly calibrate the VELO detector, it is vital to study the individual and average response of the pixels, the nature of their differences, if any, and what the next requirements for a successful calibration are. The present research will delve into these subjects by studying the charged particle flux spectra of each individual and average pixel, resultant from the controlled radiation of a monochromatic Fe55 source for a range of thresholds.

2 Theory

A mathematical formulation of the measured VELO calibration spectra is needed. For a monochromatic source of energy $E0$, the spectrum $I(E)$ follows a normal distribution

$$I(E) = \frac{1}{s\sqrt{2\pi}} e^{-\frac{1}{2}\left(\frac{E-E0}{s}\right)^2}, \tag{1}$$

where E is the threshold energy and s is the detector resolution. Pixels neighbouring a struck one will detect a fraction f of the charge going through it. This phenomena is known as charge sharing and is dealt with by correcting Eq. 1 into

$$I(E) = f \cdot \frac{1}{2}\mathbf{erfc}\left(\frac{E-E0}{s}\right) + (1-f) \cdot \frac{1}{s\sqrt{2\pi}} e^{-\frac{1}{2}\left(\frac{E-E0}{s}\right)^2}, \tag{2}$$

where **erfc** is the complementary error function. The VELO detects all particle hits above the threshold energy. In accordance, the final adjustment to Eq. 2 is done by integrating from the threshold energy to infinity, yielding the charged particle flux spectrum F

$$\begin{aligned} F(E) = Af \cdot \frac{1}{2}\left(\frac{s}{\sqrt{\pi}} e^{-\left(\frac{E-E0}{s}\right)^2} + (E0-E) \cdot \mathbf{erfc}\left(\frac{E-E0}{s}\right)\right) \\ + A(1-f) \cdot \frac{1}{s\sqrt{8\pi}} \cdot \mathbf{erfc}\left(\frac{E-E0}{s\sqrt{2}}\right), \end{aligned} \tag{3}$$

where A is a normalization factor. In light of the fact that the striking particles originate from a monochromatic radiation source, the spectrum I is equivalent to F by a proportionality factor, which is absorbed by the normalization factor. The above derivations were obtained from [10].

3 Method

3.1 Data sets

With the intention of calibrating the VELO detector, Galati, M.D., from the Groningen LHCb team, recorded the monochromatic Fe55 radiation threshold energy spectra on the pixels of an arbitrary ASIC from the VELO. The iron source's emissions were composed of 5.19 keV electrons, 5.9 keV non-ionizing X-rays and lower energy particles. Considering the lower energy particles do not exceed the thresholds and the X-rays are non-ionizing, the pixels solely document the electron hits.

Four data sets with different shutter or exposure times and number of acquisitions were compiled, of which two sets had an active cooling on the detector. The files in each data set contain 256x256 matrices, describing the amount of hits on each pixel for each acquisition and threshold. See Table 1 for a wider description of the data sets.

Table 1: Details concerning the four data sets. The shutter time (ST), number of acquisitions (nacq) and amount of thresholds used are multiplied together to find the total exposure time. The latter is indicative of the quantity of data obtained. Note that not all thresholds and acquisitions are used, for reasons explained in Sec. 3.2.

Set	Cooling	ST	nacq	Thresholds	Total time (h)
1	yes	1s 310ms	100	56	2.04
2	yes	5s 242ms	100	100	14.56
3	no	1s 310ms	25	80	0.73
4	no	20s 971ms	100	60	34.95

3.2 Data processing

The first objective is to curate the aforementioned data sets into the flux of particles on each pixel for each threshold. Good care needs to be placed in filtering the good data from the bad. In particular, 184 pixels on the subject ASIC are considered faulty and masked (see [11] for details on the masking process and conditions). Additionally, for some unknown reasons, a number of the data acquisitions prove to be defective, as the rightmost columns of the pixel grid measure exceptionally high fluxes. The acquisitions whose flux on pixels of the rightmost columns exceed an arbitrary cut value, set to two hits per second in this research, are eliminated. The flux on the pixels per threshold can now be computed by adding all the hits on a threshold and dividing by the number of good acquisitions times the shutter time. The total hits per threshold is found by adding the hits on the individual pixels.

Lastly, a portion of the data points will cause issues in the fitting process. Various pixels on the grid, in the regions further from the radioactive source predominantly, remain untouched by the radiation for some or all thresholds. If no hits are observed for more than an arbitrary amount of thresholds, 80% of the total thresholds in this research, the pixel is masked altogether. The remaining zeroes in the fluxes are trimmed. Furthermore, for some data sets and thresholds, all of the acquisitions were bad, for they measured exceptionally high fluxes, as explained in the prior paragraph. In these cases, all the smaller thresholds are trimmed as well.

3.3 Analysis

The fluxes are fitted to Eq. 3 in a number of ways. First, the fit to the total flux on the pixel grid is found. Subsequently, the fit to the fluxes on each pixel are computed twice, once fixing the $E0$, f and s parameters to the values obtained from the previous fit and once without any fixing. The chi square (χ^2) is determined for all of these cases, to ascertain the goodness of fit, by using the following equation

$$\chi^2 = \sum_i \left(\frac{O_i - E_i}{U_i} \right)^2, \tag{4}$$

where O is the observed flux, E is the fitted flux and U is the uncertainty of the observed flux.

Complications in the fitting process may arise and are dealt with by masking the relevant pixels. Such is the case when the fit could not converge for the given data, when the fit fails the chi square goodness of fit test and when the values of the fitted parameters are negative, which is not physically possible. The test is failed when the χ^2 is higher than the critical χ^2, which depends on the confidence value, 95% in this research, and the degrees of freedom for the fit. The latter differs for each pixel, for different amounts of data points are used after the trimming.

4 Results

In the current section, the spectra of some arbitrary pixels, the quality of fit performed on each pixel and a heat map of the $E0$, f and s values are illustrated. These figures are shown for the case of the most significant data set, on account of conciseness. The second and fourth data sets have the most significant amount of data; however, the latter has the most amount of data cut and lowest resulting threshold range for the reasons explained in Sec. 3.2. Henceforth, the second data set is considered.

4.1 Average and individual spectra

Two arbitrary pixels are chosen to illustrate the individual and average particle flux spectra and its respective fits, shown in Figs. 3 and 4, where DAC is an arbitrary unit for the threshold charge. Most noticeable in the below figures is the sudden decrease in flux for the individual pixels' spectra, near 1580 DAC in Fig. 3 and 1550 DAC in Fig. 4. The flux drop occurs at a different threshold for each pixel, hence eliminating the feature in the average spectrum. Another notable quality of the spectra is their scale difference. Pixels close to the radioactive source, such as pixel 127x151 in Fig. 3, experience a higher particle flux than pixels further away, such as pixel 207x119 in Fig. 4. If that is their only dissimilitude, the normalization factor in Eq. 3 ought to properly scale the fit to the average spectrum to match the individual one. Nevertheless, the lack of abrupt changes in the average flux is responsible for the failure of the fixed fit, where the characteristic distribution of the average flux cannot emulate the flux of the individual pixels. The free fit, on the contrary, is allowed to properly describe the individual fluxes and, thence, finds a higher success rate.

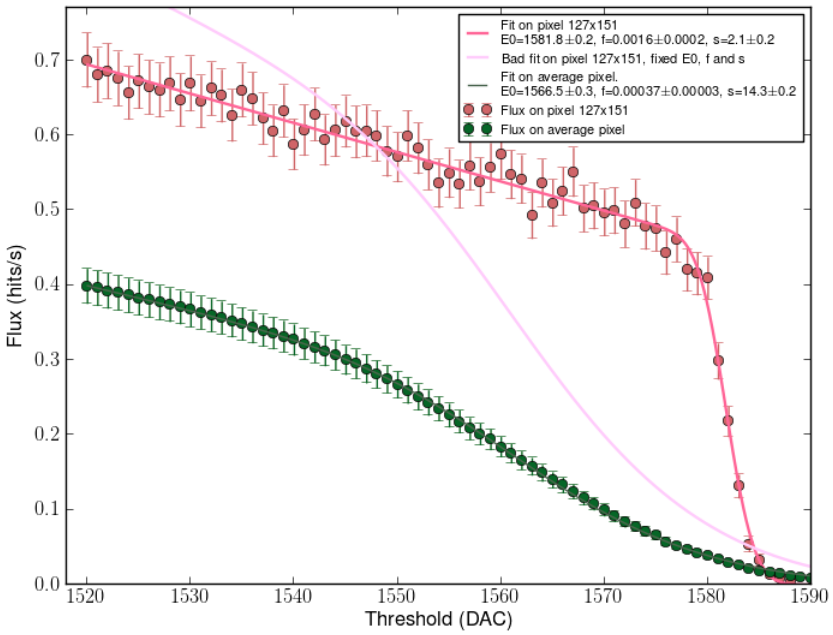

Figure 3: Spectra of average and pixel 127x151, from the second data set. DAC is an arbitrary unit for the threshold charge

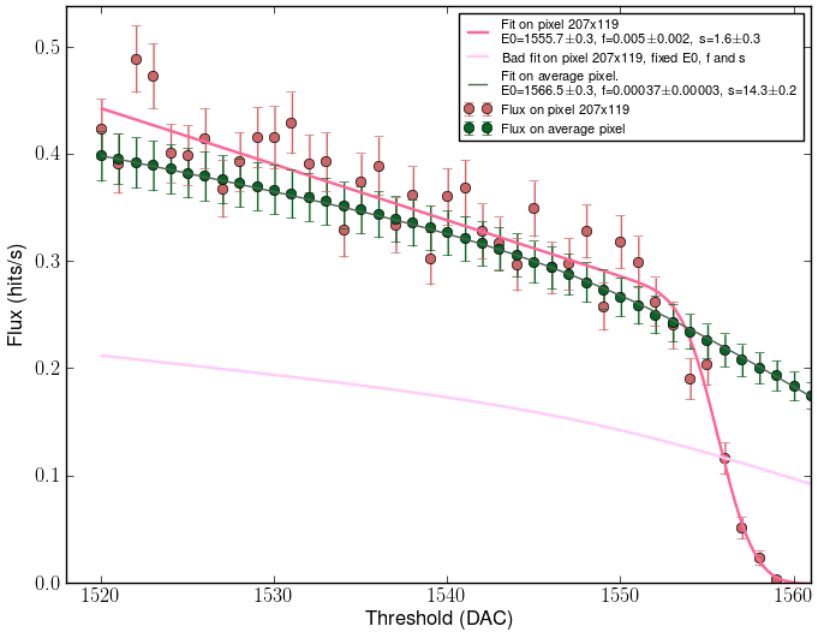

Figure 4: Spectra of average and pixel 207x119, from the second data set. DAC is an arbitrary unit for the threshold charge

4.2 $E0$, f and s heat maps

To further explore the differences between the average and individual spectra, the heat maps with the fitted values of $E0$, f and s for the second data set are depicted in Figs. 5-7. From these, it is found that the average values of the fitted parameters are $E0 = 1561.055 \pm 0.002$ DAC, $f = (1695 \pm 3) \cdot 10^{-6}$ and $s = (2405 \pm 3) \cdot 10^{-8}$, whereas the values of the parameters from the fit to the average spectrum, which may be found in the legend in Fig. 3 or 4, are $E0 = 1566.5 \pm 0.3$ DAC, $f = (37 \pm 3) \cdot 10^{-5}$ and $s = 14.3 \pm 0.2$. Comparing these results, it is remarked that both $E0$s lie in the vicinity of each other. The f parameter is an order of magnitude higher for the individual spectra. Given the lightness of the electrons and the small size of the pixels, for electrons of 5.19 keV, the amount of charge sharing is comparable, if not lower, to that predicted by [12]. Howbeit, the dominant difference between the average and individual spectra is the contrast between both s parameters, which is six orders of magnitude lower for the individual spectra. The parameter s in Eq. 3 is responsible for the sudden drop in flux; consequently, the disparity in s between the average and individual spectra provides a quantitative description of their difference. When calculating the average spectrum, the characteristic drop in flux is erased by the spectra that experience the drop at other thresholds, thus increasing the value of s. The $E0$, f and s heat maps for the first, third and fourth data sets may be found in Figs. 10-18, in Sec. A.

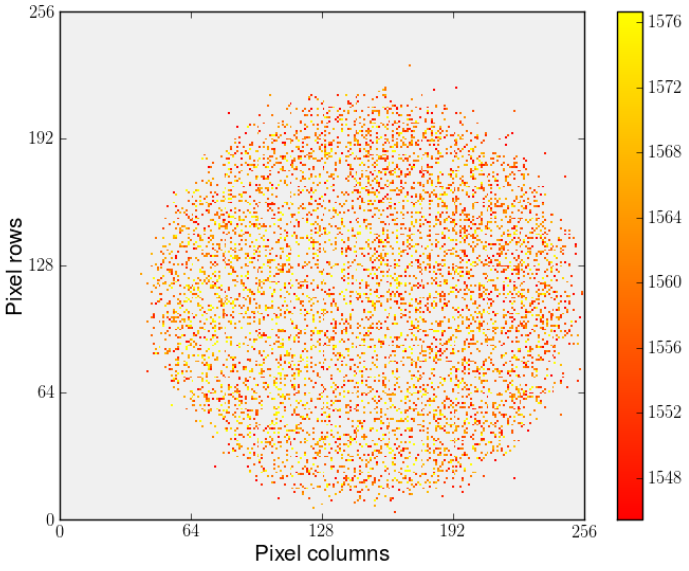

Figure 5: Pixel grid illustrating the $E0$ parameter, from the second data set. The average is $E0 = 1561.055 \pm 0.002$ DAC. Note that the limits in the color bar are not equivalent to the data range.

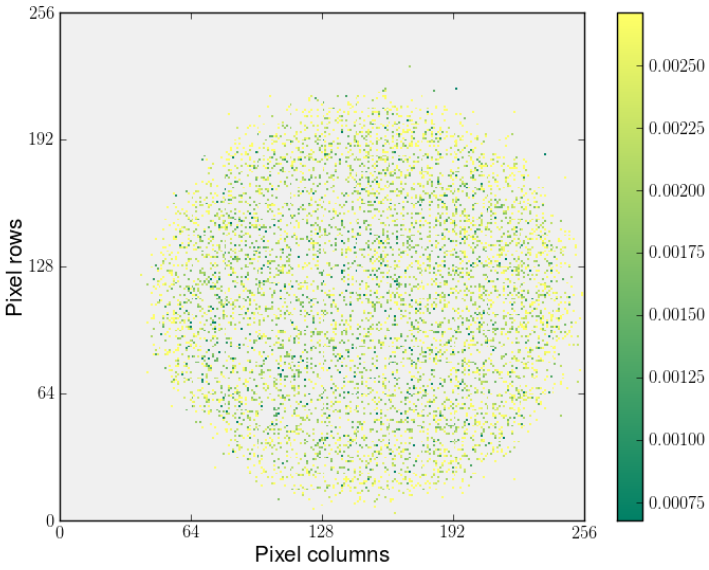

Figure 6: Pixel grid illustrating the f parameter, from the second data set. The average is $f = (1695 \pm 3) \cdot 10^{-6}$. Note that the limits in the color bar are not equivalent to the data range.

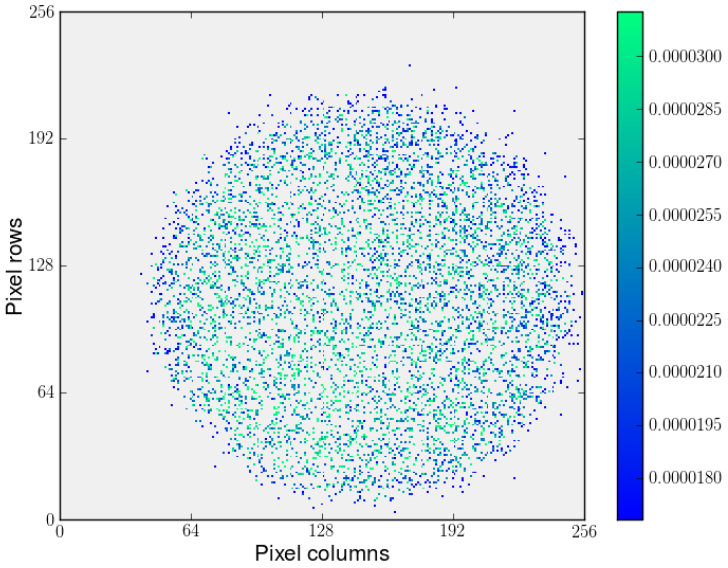

Figure 7: Pixel grid illustrating the f parameter, from the second data set. The average is $s = (2405 \pm 3) \cdot 10^{-8}$. Note that the limits in the color bar are not equivalent to the data range.

4.3 Quality of fit heat maps

The quality of the free and fixed fits per pixel, using the second data set, is showcased in Figs. 8 and 9. There, four scenarios can be observed in the color bar. "Good fit" is for the fits that passed the chi square test, "Bad fit" represents the fits that failed the chi square test or found negative values for the $E0$, f or s parameters, "Fit not found" stands for the fits that could not converge and "Cut data" represents the pixels that were masked before the fitting process. The corresponding figures for the first, third and fourth data sets may be found in Figs. 19-24, in Sec. A.

From the below figures, the success of the fixed and free fits is discerned. Fig. 8 shows that none of the pixels find a good fit, whereas Fig. 9 reveals that 6410 pixels out of 65536 ($\sim 9.78\%$) find a good fit, further providing evidence for the dissimilitude between the average and individual spectra.

Moreover, both figures exhibit circular shapes for the different categories of fits. Indeed, the further the pixels are located from the radioactive source, the less particle hits they record. Most interesting is the fact that the good fits in Fig. 9 form a circle at the center of the grid, which is the region closest to the source. This indicates that the pixels in this area, having recorded more hits, are better able to find a good fit and that pixels further away are unable to find a good fit due to a lack of data. Supplemental evidence for this argument is the fact that, for the first and third data sets, which have the lowest total exposure times, only 3532 ($\sim 5.39\%$) and 697 ($\sim 1.06\%$) pixels respectively, find a good fit. For the fourth data set, which has the longest total exposure time, 9600 ($\sim 14.6\%$) pixels resulted in a good fit; however, the fourth data set is the one with most data eliminated and lowest resulting threshold range. Hence, its precision might be affected by this.

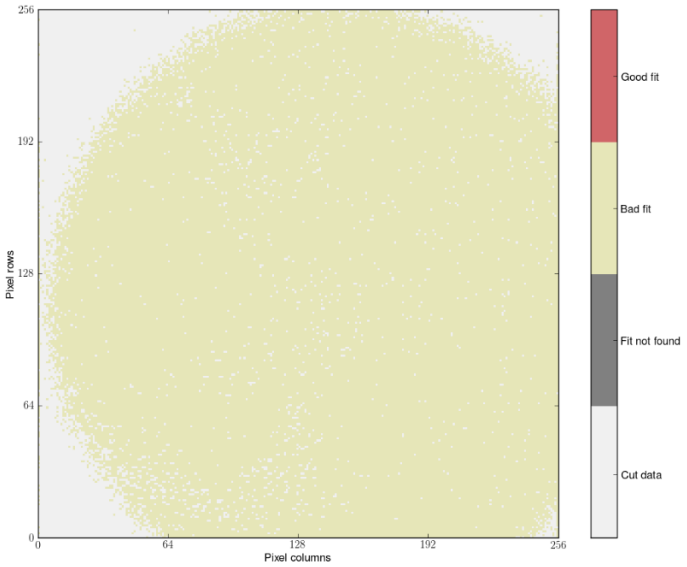

Figure 8: Pixel grid showcasing the quality of fit per pixel for the second data set, fixing $E0 = 1566.5$ DAC, $f = 3.7 \cdot 10^{-4}$ and $s = 14.3$, the values from the average spectrum fit. Out of 65536 pixels, 0 resulted in a good fit, 55170 ($\sim 84.2\%$) in a bad fit, 0 did not receive any fit and 10366 ($\sim 15.8\%$) were masked before the fitting process.

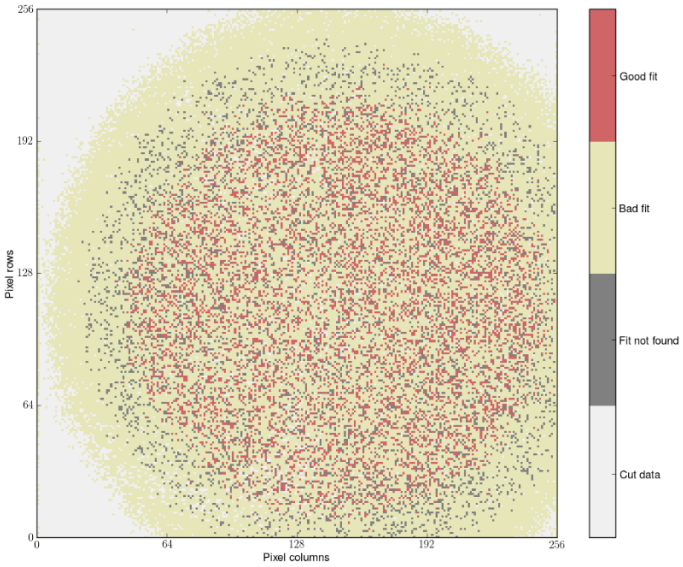

Figure 9: Pixel grid showcasing the quality of fit per pixel for the second data set, without fixing the parameters. Out of 65536 pixels, 6410 ($\sim 9.78\%$) resulted in a good fit, 43418 ($\sim 66.3\%$) in a bad fit, 5342 ($\sim 8.15\%$) did not receive any fit and 10366 ($\sim 15.8\%$) were masked before the fitting process.

5 Discussion

The present research intends to investigate the differences between the individual and average pixels, the nature of their disparities, if any, and what the next requirements to properly calibrate the pixels of the VELO detector are. These queries are discussed in light of the foregoing results.

Studying the individual and average spectra in Figs. 3 and 4 manifests their dissimilitude, which is mainly the sudden drop in flux for the individual spectrum and the lack thereof for the average spectrum. As is demonstrated by Figs. 5-7, the s parameter, which controls this feature, is responsible for their discrepancy, finding a value six orders of magnitude lower for the individual spectra. Given that the flux drop occurs at different thresholds, the trait is eliminated in the average spectrum. Figs. 8 and 9 further reveal the disparity between both spectra, where, by leaving the parameters free, a fit that passes the chi square test for almost 10% of the pixels' spectra is found. In contrast, fixing the parameters to those obtained from the fit to the average spectrum causes all the individual spectra fits to fail the chi square test.

Owing to the heterogeneity of the pixels, a general calibration of the pixels of the VELO detector is imprudent; rather, an individual calibration of the pixels is justified. Furthermore, observing Figs. 8 and 9 and the amount of good fits from the other data sets indicates a qualitative relation between the quality of fits and the total exposure time. The amount of exposure time for a proper calibration is out of the scope of this research; be that as it may, considering that approximately 14.5 hours of exposure resulted in only nearly 10% of the pixels finding a good fit, it is clear that a much longer exposure time to the monochromatic radiation Fe55 source is warranted. Alternatively, a more active radiation source may be used to accumulate hits faster.

In consideration of the above results and discussion points, the charged particle flux spectra through the individual pixels do not resemble that of the average, presumptively due to the pixels' small resolution, which is not represented in the average spectrum. This verdict supports the need for individual pixel calibrations. Further calibration measurements with greater exposure times are needed to support these conclusions and advance the VELO's calibration process.

6 Conclusion

In the pursuit of studying the fundamental particles of the universe and their interactions, the LHCb is studying b and c hadron decays in the hopes of better understanding the baryon asymmetry problem. One of the observables it needs to distinguish a signal from background is the impact parameters and location of the primary and secondary vertices of the pp interaction, accelerated by the LHC. For that purpose, the VELO detector is set next to the interaction region and was recently replaced by a new silicon pixel version. The current challenge lies in properly calibrating the pixels in the detector.

The current study investigates the similitude of the pixels and the next steps in the VELO calibration process by examining the charged particle flux through the pixels of an arbitrary ASIC, resultant from the radiation of a monochromatic radioactive Fe55 source. In addition, the nature of their heterogeneity is explored.

Four data sets were available from the radiation threshold scan. After trimming the bad acquisitions and thresholds with no hits, the spectra were fitted to Eq. 3. From this, the spectra comparisons, chi square tests, quality of fit heat maps and $E0$, f and s values were computed, masking the pixels that were initially considered faulty, had too many zero-hits or received no or a bad fit.

Ensuing the results, answers to the research goals are considered. The spectra of the individual pixels are dissimilar to that of the average spectrum, principally by reason of a sharp drop in flux for the individual spectra, quantitatively described by a resolution six orders of magnitude lower than that of the average spectrum. On that account, the VELO detector requires an individual calibration of its pixels, rather than a general calibration of the pixel grid. Furthermore, by virtue of the limited exposure time for each data set and, consequently, the lack of hits, very few fits are able to pass the χ^2 test. Continuing the VELO calibration, longer exposure times to a radioactive source are incumbent.

References

[1] E. Grant, *A history of natural philosophy: From the ancient world to the nineteenth century*. Cambridge University Press, 2007.

[2] J. J. Thomson, "Xl. cathode rays," *The London, Edinburgh, and Dublin Philosophical Magazine and Journal of Science*, vol. 44, no. 269, pp. 293–316, 1897.

[3] A. Pais and S. Treiman, "How many charm quantum numbers are there?," *Physical Review Letters*, vol. 35, no. 23, p. 1556, 1975.

[4] T. Kajita, "Discovery of atmospheric neutrino oscillations," *Nobel Lecture*, 2015.

[5] A. B. McDonald, "The sudbury neutrino observatory: observation of flavor change for solar neutrinos," *Annalen der Physik*, vol. 528, no. 6, pp. 469–480, 2016.

[6] B. Abi *et al.*, "Measurement of the positive muon anomalous magnetic moment to 0.46 ppm," *Physical Review Letters*, vol. 126, no. 14, p. 141801, 2021.

[7] I. Belyaev, G. Carboni, N. Harnew, C. Matteuzzi, and F. Teubert, "The history of LHCb," *The European Physical Journal H*, vol. 46, no. 1, p. 3, 2021.

[8] K. Hennessy, "LHCb VELO upgrade," *Nuclear Instruments and Methods in Physics Research Section A: Accelerators, Spectrometers, Detectors and Associated Equipment*, vol. 845, pp. 97–100, feb 2017.

[9] T. Poikela *et al.*, "The velopix asic," *Journal of Instrumentation*, vol. 12, p. C01070, jan 2017.

[10] M. D. Galati. "personal communication", 2023.

[11] S. Bakker, "The velopix upgrade for the lhcb experiment," 2021.

[12] K. Mathieson *et al.*, "Charge sharing in silicon pixel detectors," *Nuclear Instruments and Methods in Physics Research Section A: Accelerators, Spectrometers, Detectors and Associated Equipment*, vol. 487, no. 1-2, pp. 113–122, 2002.

A Appendix

Hereafter are the $E0$, f and s heat maps for the first, third and fourth data set, in Figs. 10-12, 13-15 and 16-18. Subsequently, the quality of fit heat maps are found in Figs. 19-24.

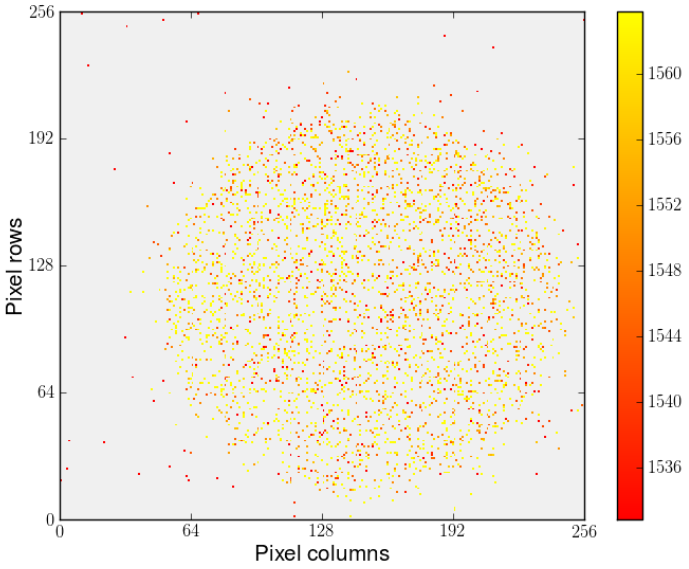

Figure 10: Pixel grid illustrating the $E0$ parameter, from the first data set. The average is $E0 = 1548.33 \pm 0.02$ DAC. Note that the limits in the color bar are not equivalent to the data range.

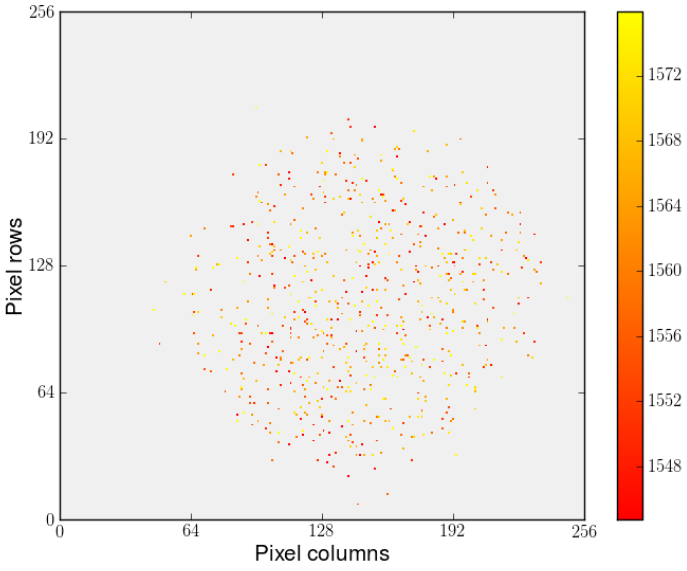

Figure 11: Pixel grid illustrating the $E0$ parameter, from the first data set. The average is $E0 = 1560.34 \pm 0.03$ DAC. Note that the limits in the color bar are not equivalent to the data range.

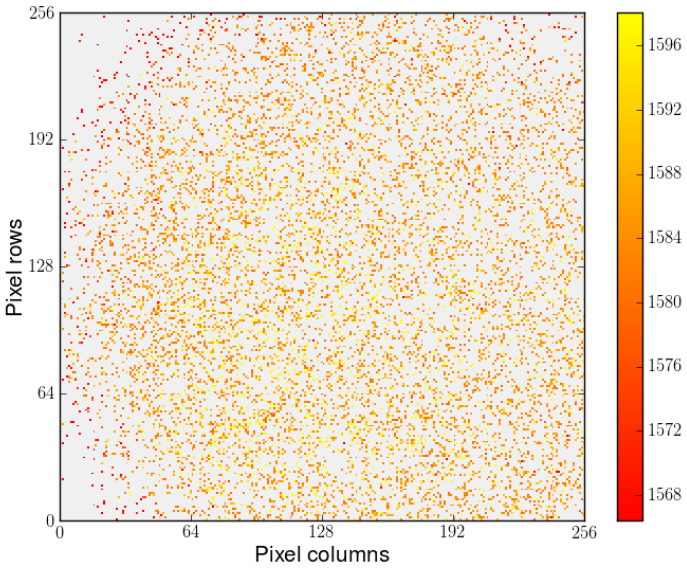

Figure 12: Pixel grid illustrating the $E0$ parameter, from the first data set. The average is $E0 = 1582.237 \pm 0.0002$ DAC. Note that the limits in the color bar are not equivalent to the data range.

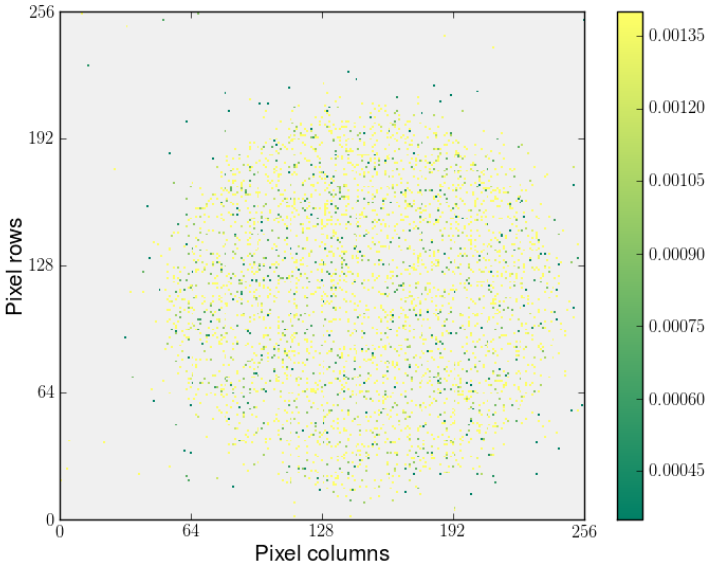

Figure 13: Pixel grid illustrating the f parameter, from the first data set. The average is $f = (875 \pm 7) \cdot 10^{-6}$. Note that the limits in the color bar are not equivalent to the data range.

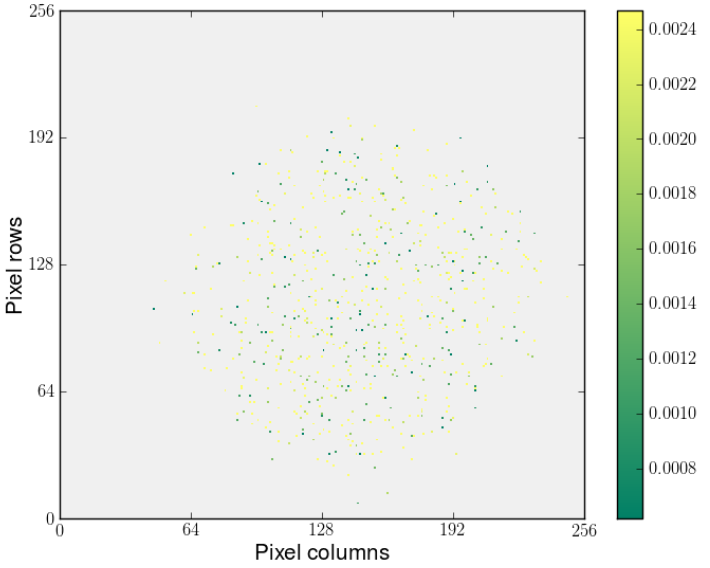

Figure 14: Pixel grid illustrating the f parameter, from the third data set. The average is $f = (154 \pm 4) \cdot 10^{-5}$. Note that the limits in the color bar are not equivalent to the data range.

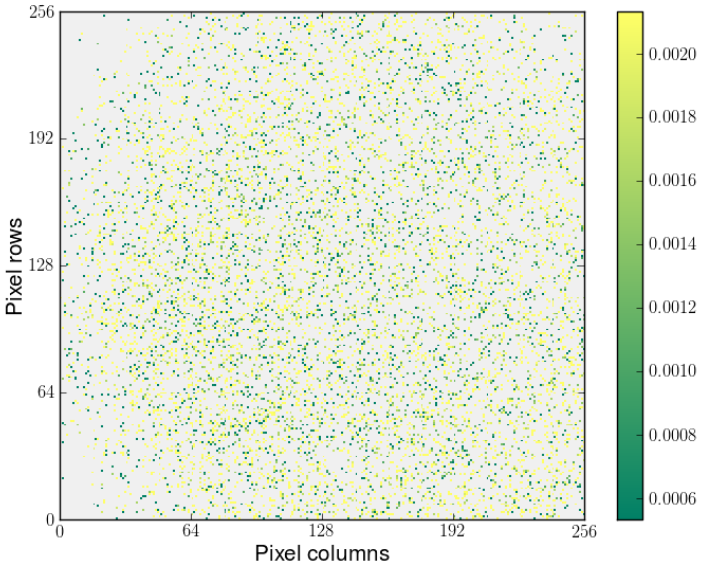

Figure 15: Pixel grid illustrating the f parameter, from the fourth data set. The average is $f = (13326 \pm 4) \cdot 10^{-7}$. Note that the limits in the color bar are not equivalent to the data range.

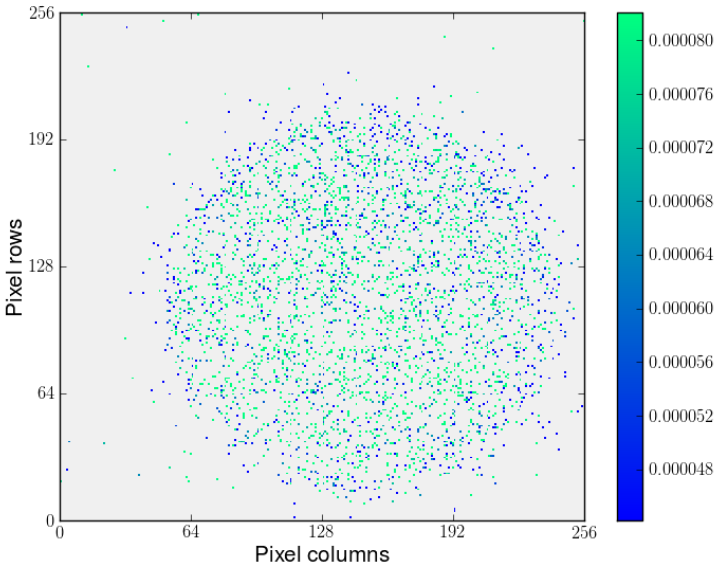

Figure 16: Pixel grid illustrating the s parameter, from the first data set. The average is $s = (631 \pm 4) \cdot 10^{-7}$. Note that the limits in the color bar are not equivalent to the data range.

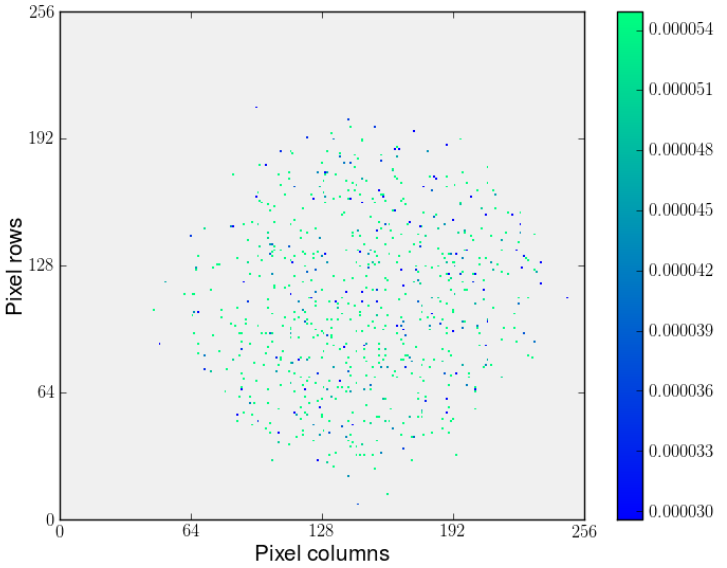

Figure 17: Pixel grid illustrating the s parameter, from the third data set. The average is $s = (423 \pm 7) \cdot 10^{-7}$. Note that the limits in the color bar are not equivalent to the data range.

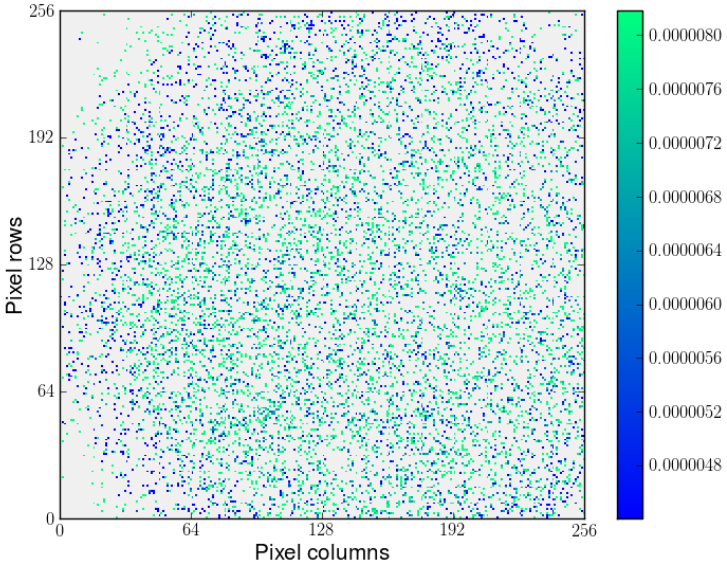

Figure 18: Pixel grid illustrating the s parameter, from the fourth data set. The average is $s = (62960 \pm 3) \cdot 10^{-10}$. Note that the limits in the color bar are not equivalent to the data range.

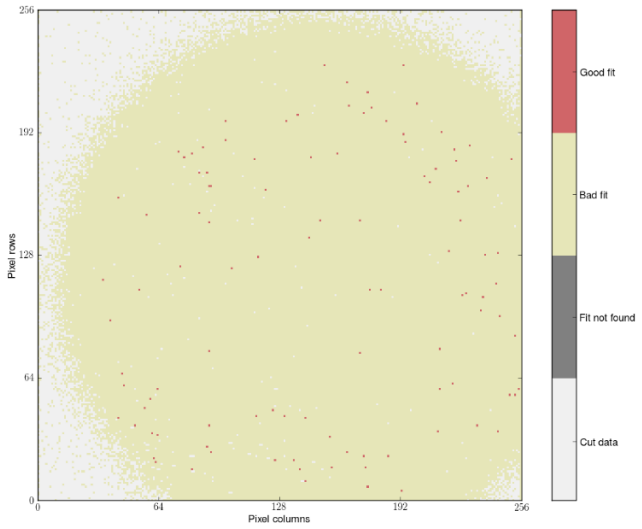

Figure 19: Pixel grid showcasing the quality of fit per pixel for the first data set, fixing $E0 = 1577$ DAC, $f = 3 \cdot 10^{-3}$ and $s = 13$, the values from the average spectrum fit. Out of 65536 pixels, 106 ($\sim 0.16\%$) resulted in a good fit, 55465 ($\sim 84.6\%$) in a bad fit, 0 did not receive any fit and 9965 ($\sim 15.2\%$) were masked before the fitting process.

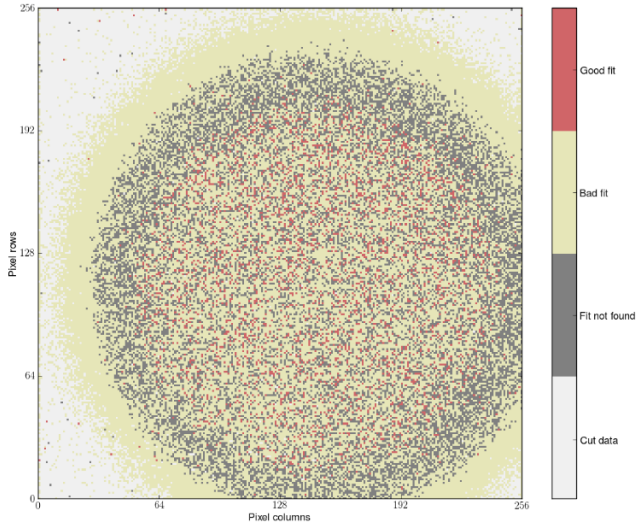

Figure 20: Pixel grid showcasing the quality of fit per pixel for the first data set, without fixing the parameters. Out of 65536 pixels, 3532 ($\sim 5.39\%$) resulted in a good fit, 37177 ($\sim 56.7\%$) in a bad fit, 14862 ($\sim 22.3\%$) did not receive any fit and 9965 ($\sim 15.2\%$) were masked before the fitting process.

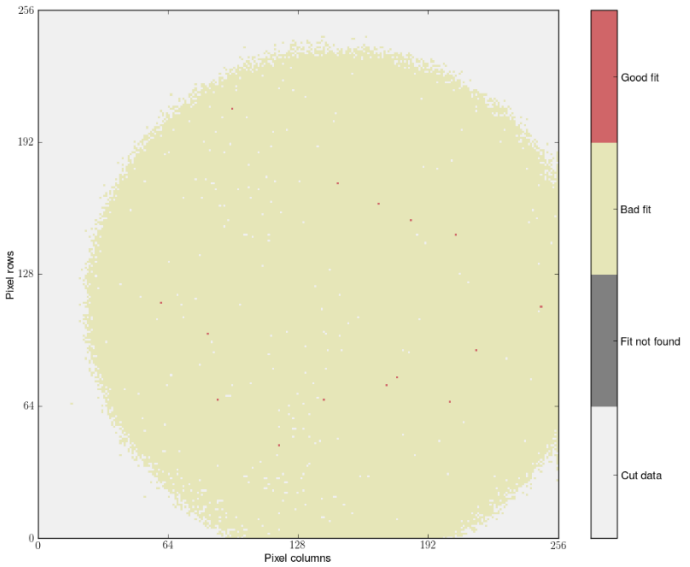

Figure 21: Pixel grid showcasing the quality of fit per pixel for the third data set, fixing $E0 = 1576.2$ DAC, $f = 92 \cdot 10^{-5}$ and $s = 12.7$, the values from the average spectrum fit. Out of 65536 pixels, 15 ($\sim 0.02\%$) resulted in a good fit, 46217 ($\sim 70.5\%$) in a bad fit, 0 did not receive any fit and 19304 ($\sim 29.5\%$) were masked before the fitting process.

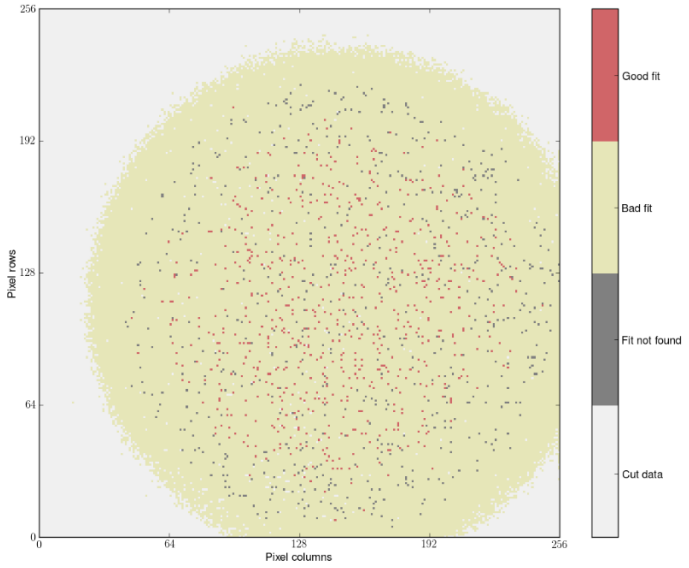

Figure 22: Pixel grid showcasing the quality of fit per pixel for the third data set, without fixing the parameters. Out of 65536 pixels, 697 ($\sim 1.06\%$) resulted in a good fit, 44906 ($\sim 68.5\%$) in a bad fit, 629 ($\sim 0.96\%$) did not receive any fit and 19304 ($\sim 29.5\%$) were masked before the fitting process.

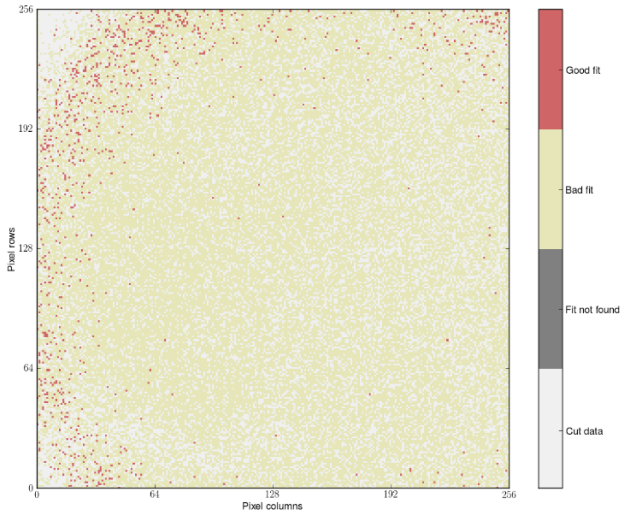

Figure 23: Pixel grid showcasing the quality of fit per pixel for the fourth data set, fixing $E0 = 1564$ DAC, $f = 4 \cdot 10^{-4}$ and $s = 18$, the values from the average spectrum fit. Out of 65536 pixels, 944 ($\sim 1.44\%$) resulted in a good fit, 42950 ($\sim 65.5\%$) in a bad fit, 0 did not receive any fit and 21642 ($\sim 33.0\%$) were masked before the fitting process.

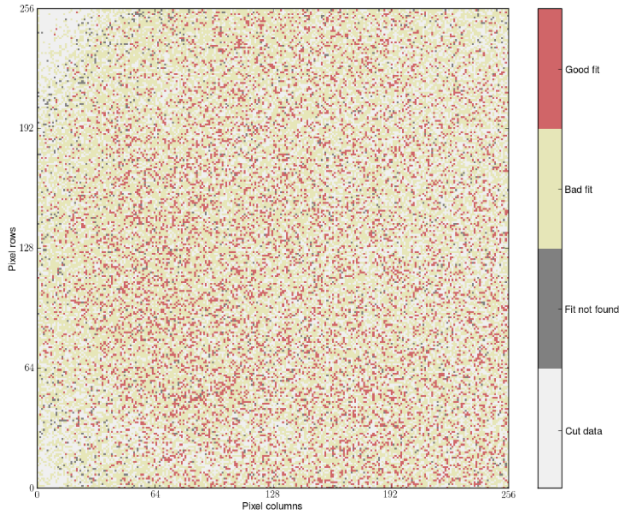

Figure 24: Pixel grid showcasing the quality of fit per pixel for the fourth data set, without fixing the parameters. Out of 65536 pixels, 9600 ($\sim 14.6\%$) resulted in a good fit, 32821 ($\sim 50.1\%$) in a bad fit, 1473 ($\sim 2.25\%$) did not receive any fit and 21642 ($\sim 33.0\%$) were masked before the fitting process.